

## Quantitative accordance of Dzyaloshinskii-Moriya interaction between domain-wall and spin-wave dynamics

Dae-Yun Kim,<sup>1,2</sup> Nam-Hui Kim,<sup>3</sup> Yong-Keun Park,<sup>1,2</sup> Min-Ho Park,<sup>2</sup> Joo-Sung Kim,<sup>2</sup> Yune-Seok Nam,<sup>2</sup> Jinyong Jung,<sup>3</sup> Jaehun Cho,<sup>4</sup> Duck-Ho Kim,<sup>1,5</sup> June-Seo Kim,<sup>6</sup> Byoung-Chul Min,<sup>1</sup> Sug-Bong Choe,<sup>2,\*</sup> and Chun-Yeol You<sup>3,†</sup>

<sup>1</sup>Center for Spintronics, Korea Institute of Science and Technology (KIST), Seoul, 02792, Republic of Korea


<sup>2</sup>Department of Physics and Astronomy, Seoul National University, Seoul, 08826, Republic of Korea

<sup>3</sup>Department of Emerging Materials Science, Daegu Gyeongbuk Institute of Science and Technology (DGIST), Daegu, 42988, Republic of Korea

<sup>4</sup>Global Center for Bio-Convergence Spin System, DGIST, Daegu 42988, South Korea

<sup>5</sup>Institute for Chemical Research, Kyoto University, Kyoto, 611-0011, Japan

<sup>6</sup>Intelligent Devices & Systems Research Group, Institute of Convergence, DGIST, Daegu, 42988, Korea

 (Received 3 March 2019; revised manuscript received 10 October 2019; published 20 December 2019)

The magnetic exchange interaction is one of the key factors governing the basic characteristics of magnetic systems. In contrast to the symmetric nature of the Heisenberg exchange interaction, the interfacial Dzyaloshinskii-Moriya interaction (DMI) generates an antisymmetric exchange interaction, which offers challenging opportunities in spintronics with intriguing antisymmetric phenomena. The role of the DMI, however, is still under debate, because largely distinct strengths of the DMI have been measured for different magnetic objects, particularly chiral magnetic domain walls (DWs) and nonreciprocal spin waves (SWs). In this paper, by carefully examining the measurement principles, we demonstrate that both the DWs and SWs experience the same strength of the DMI. The key factor in this demonstration is to identify the appropriate experimental conditions by excluding all possible artifacts that causes additional undesired symmetric and antisymmetric contributions in chiral DW dynamics. The present demonstration, therefore, verifies the universality of the DMI between different magnetic dynamics as an intrinsic exchange interaction and also, guarantees the compatibility of several DMI-measurement schemes recently proposed.

DOI: [10.1103/PhysRevB.100.224419](https://doi.org/10.1103/PhysRevB.100.224419)

### I. INTRODUCTION

The interfacial Dzyaloshinskii-Moriya interaction (DMI) is an antisymmetric exchange interaction between spins, mediated by heavy-metal atoms [1–3]. It is known that structural inversion asymmetry in magnetic systems generates the DMI with an energy  $E_{\text{DMI}}$  in the form of

$$E_{\text{DMI}} = -\vec{D} \cdot (\vec{M}_i \times \vec{M}_j), \quad (1)$$

where  $\vec{D}$  is the DMI vector and  $\vec{M}_i$  and  $\vec{M}_j$  are the neighboring local magnetizations. The DMI-induced antisymmetric exchange interaction has recently received great attention because of its crucial role in spintronic materials, such as the stabilization of chiral magnetic domain walls (DWs) or the formation of magnetic skyrmions [4–7]. Numerous efforts have been devoted to investigate the role of the DMI on the magnetization process [6–8] and also, various experimental schemes to quantify the DMI strengths have been proposed [9–31]. These experimental schemes are mainly based on either the DMI-induced chirality of the DWs [9–14] or the DMI-induced nonreciprocity of the spin waves (SWs) [15–31].

Up to now, however, the measurement results among these experimental schemes have been in conflict. The DMI strengths measured by different schemes show huge discordance with each other [23]. This discordance is one of the most urgent and important issues that must be solved from academic and technological points of view. In the academic point of view, the discordance raises the question of whether the DMI has an intrinsic characteristic independent of the magnetic situations. Also, in the technical point of view, such discordance does not allow unambiguous determination of the DMI strength, resulting in poor reliability of the DMI measurement schemes. It is not yet clear whether the discordance comes from the nature of different magnetic situations or from technical deficiencies in the measurement schemes.

Therefore, here we examined the DMI strengths in different magnetic situations of DW and SW dynamics, by employing three different measurement schemes based on the reciprocal SW propagation, field-induced DW motion, and current-induced DW motion. By taking into account the dynamic characteristics and excluding possible artifacts of each scheme, accordance between the DMI strengths of different measurement schemes could be achieved with optimal experimental conditions for each scheme and finally, the hierarchy of the most appropriate schemes is proposed in terms of the ferromagnetic layer thickness and the DMI strength.

\*sugbong@snu.ac.kr

†cyyou@dgist.ac.kr

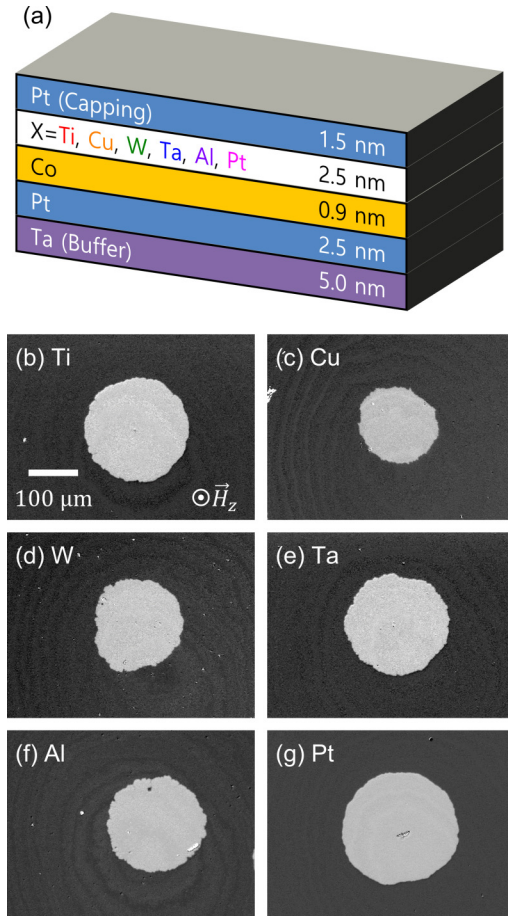


FIG. 1. (a) Schematic drawing of the layered structure for the series of Pt/Co/X films. (b)–(g) Magneto-optical Kerr effect images of magnetic domain for the series of Pt/Co/X films with different X as denoted inside each panel.

## II. SAMPLE PREPARATION

For this study, a series of Pt/Co/X films with different X (=Al, Au, Cu, Pt, Ta, Ti, and W) was prepared by DC magnetron sputtering. The films were deposited on Si/SiO<sub>2</sub> substrates with a 5.0-nm-thick Ta adhesion layer and 1.5-nm-thick Pt protection layer. The detailed layer structure was 2.5-nm Pt/0.9-nm Co/2.5-nm X as illustrated in Fig. 1(a). This Co layer thickness was chosen to meet all the experimental requirements of each DMI measurement scheme: The DW-based scheme requires thin ferromagnetic layers that are thin enough to ensure clear DW motion, whereas the SW-based scheme requires thick ferromagnetic layers that are thick enough to ensure the sensitivity in the Brillouin light-scattering (BLS) measurement. All the films exhibit strong perpendicular magnetic anisotropy (PMA) and clear DW expansion under application of out-of-plane magnetic field, resulting in large circular domains as seen by the magneto-optical Kerr effect images in Figs. 1(b)–1(g).

## III. MEASUREMENT OF DMI STRENGTH ON SWs

We first examined the DMI strength on SWs, by employing the BLS-measurement [15–31] for the series of films. We will

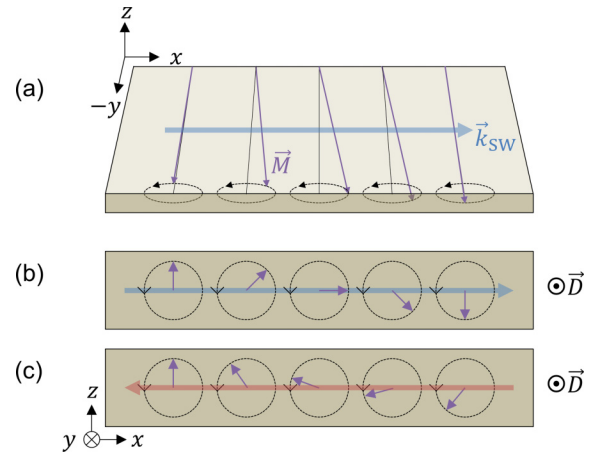


FIG. 2. (a) Schematic diagram of the DE-mode geometry. The black curved arrows show the direction of counterclockwise precession. The purple arrows show the local magnetization. The blue arrow shows the wave vector  $\vec{k}_{\text{SW}}$ . (b), (c) Cross-sectional view of the SWs propagating along the  $+\hat{x}$  (blue arrow) and  $-\hat{x}$  (red arrow) directions, respectively. The purple arrows show the local magnetization at precession. The black circles with arrows show the direction of precession.

denote this measurement scheme as “BLS scheme” hereafter. In the BLS measurement geometry, the DMI mainly interacts with the surface SW mode—the so-called Damon-Eshbach (DE) mode [32]—among the various SW modes. In the DE mode, both the wave vector  $\vec{k}_{\text{SW}}$  and the magnetization  $\vec{M}$  lie in the film plane along the directions orthogonal to each other as depicted in Fig. 2(a). In experiments, an in-plane magnetic field  $H_y$ —sufficiently stronger than the anisotropy field  $H_K$ —was applied along the  $-\hat{y}$  direction to align the magnetization in the film plane. For this situation, the magnetization precession is counterclockwise as shown by the curved black arrows in Fig. 2(a). This precession allows two SW modes with opposite propagation directions, i.e.,  $\vec{k}_{\text{SW}}$ 's. The cross-sectional views in Figs. 2(b) and 2(c) show the two SW modes with opposite  $\vec{k}_{\text{SW}}$ 's along the  $+\hat{x}$  and  $-\hat{x}$  directions, respectively.

It is worth noting that, due to the opposite propagation directions, the two SW modes have opposite angles between the local magnetizations neighboring in space as seen by Figs. 2(b) and 2(c), respectively. Therefore, values of  $\vec{M}_i \times \vec{M}_j$  are opposite to each other between the two SW modes, resulting in the opposite signs of  $E_{\text{DMI}}$  in Eq. (1) with a fixed  $\vec{D}$  in a given film. Therefore, the two SW modes have opposite DMI-induced energy shifts to each other, which results in the nonreciprocal shifts of the peak frequency.

This nonreciprocity between the SW modes was experimentally verified by Cho *et al.* [15] via the BLS measurement. Figure 3 shows the typical BLS spectrum for the present series of films, where the wave vector  $k_{\text{SW}}$  is fixed ( $=0.0167 \text{ nm}^{-1}$ ). The figure clearly shows that the shifts of the peak frequency  $\Delta f_{\text{SW}}$  appear between SW modes with the opposite wave vectors  $\pm k_{\text{SW}}$ , respectively. According to Refs. [15–18],  $\Delta f_{\text{SW}}$  is given by

$$\Delta f_{\text{SW}} = \frac{2\gamma k_{\text{SW}}}{\pi M_S} D_{\text{SW}}, \quad (2)$$

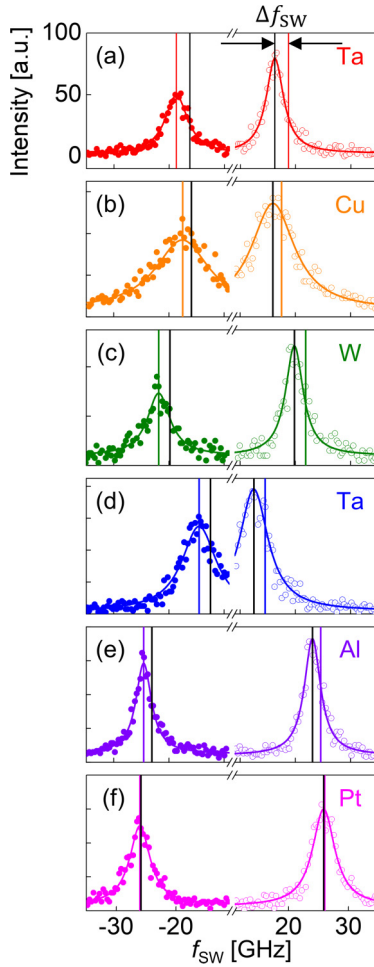


FIG. 3. BLS spectrum for the series of Pt/Co/ $X$  films with different  $X$  as denoted in each panel. The solid curves show the best Lorentzian fitting. Each panel has two colored (and black) vertical lines: one indicates the position of the peak intensity for the negative (and positive)  $f_{\text{SW}}$  regime, while the other shows its mirrored position to the origin. The black arrows indicate  $\Delta f_{\text{SW}}$  between the two peaks.

where  $\gamma$  is the gyromagnetic ratio and  $M_S$  is the saturation magnetization. Here,  $D_{\text{SW}}$  refers to the DMI strength on the SWs. By use of the typical value of  $\gamma$  ( $\cong 2.16$ ) for the bulk fcc Co [33] and measured values of  $M_S$ , the magnitudes of  $D_{\text{SW}}$  were estimated. The magnitudes of  $D_{\text{SW}}$  are listed in Table I for the series of films with different  $X$ .

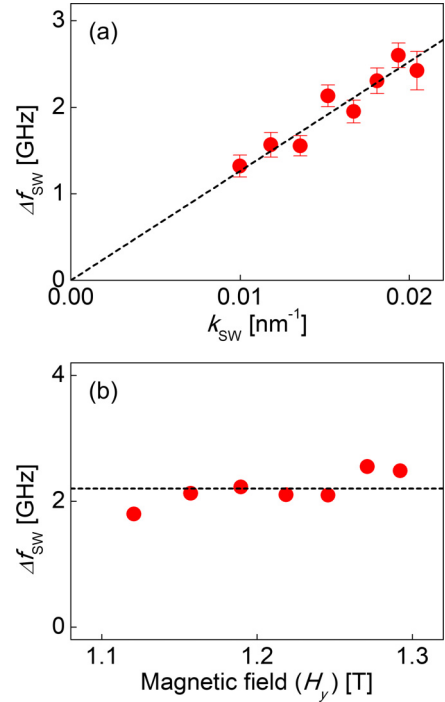


FIG. 4. (a) Plot of  $\Delta f_{\text{SW}}$  as a function of  $k_{\text{SW}}$  for the Pt/Co/Ti film. The dashed line guides the linear proportionality. (b) Plot of  $\Delta f_{\text{SW}}$  as a function of  $H_y$  for the same film. The horizontal dashed line shows the average values.

To avoid the artifacts from possible offsets in  $\Delta f_{\text{SW}}$ , both the  $H_y$  dependence and  $k_{\text{SW}}$  dependence of  $\Delta f_{\text{SW}}$  were examined. Figure 4(a) plots  $\Delta f_{\text{SW}}$  as a function of  $k_{\text{SW}}$  for the film with  $X = \text{Ti}$ . The figure clearly shows that  $\Delta f_{\text{SW}}$  is directly proportional to  $k_{\text{SW}}$  in agreement with Eq. (2). Such direct proportionality confirms that  $\Delta f_{\text{SW}}$  is mainly originated from the DMI, excluding the possible artifacts from asymmetric PMA between top and bottom interfaces. In addition, the  $H_y$  dependence of  $\Delta f_{\text{SW}}$  was also investigated. Figure 4(b) plots  $\Delta f_{\text{SW}}$  as a function of  $H_y$  for the same film. As guided by the horizontal dashed line in the figure,  $\Delta f_{\text{SW}}$  is invariant irrespective of  $H_y$ . The present observation guarantees that the DE mode is dominant over the present range of  $H_y$ .

#### IV. MEASUREMENT OF DMI STRENGTH ON DWs

We then examined the DMI strength on DWs for the same series of films, to directly compare with the DW strengths

TABLE I.  $H_K$ ,  $M_S$ ,  $\Delta f_{\text{SW}}$ ,  $D_{\text{SW}}$ ,  $H_{\text{DMI}}$ , and  $D_{\text{DW}}$ .

$X$	$H_K$ (T)	$M_S$ ( $10^6$ A/m)	$\Delta f_{\text{SW}}$ (GHz)	$D_{\text{SW}}$ (mJ/m $^2$ )	$H_{\text{DMI}}$ (mT)	$D_{\text{DW}}$ (mJ/m $^2$ )
Ti	$1.13 \pm 0.013$	$1.33 \pm 0.03$	$2.20 \pm 0.26$	$1.42 \pm 0.17$	$-197 \pm 25$	$1.42 \pm 0.19$
Cu	$0.90 \pm 0.021$	$1.14 \pm 0.01$	$1.57 \pm 0.54$	$0.87 \pm 0.40$	$-190 \pm 25$	$1.42 \pm 0.21$
W	$0.95 \pm 0.012$	$1.16 \pm 0.01$	$2.15 \pm 0.21$	$1.25 \pm 0.12$	$-183 \pm 5$	$1.35 \pm 0.05$
Ta	$1.20 \pm 0.018$	$1.02 \pm 0.01$	$1.95 \pm 0.31$	$0.99 \pm 0.16$	$-160 \pm 10$	$0.98 \pm 0.09$
Al	$0.94 \pm 0.049$	$1.38 \pm 0.02$	$1.35 \pm 0.13$	$0.92 \pm 0.09$	$-109 \pm 5$	$0.87 \pm 0.08$
Pt	$0.79 \pm 0.010$	$1.87 \pm 0.02$	$0.02 \pm 0.13$	$0.02 \pm 0.11$	$0 \pm 10$	$0.00 \pm 0.11$

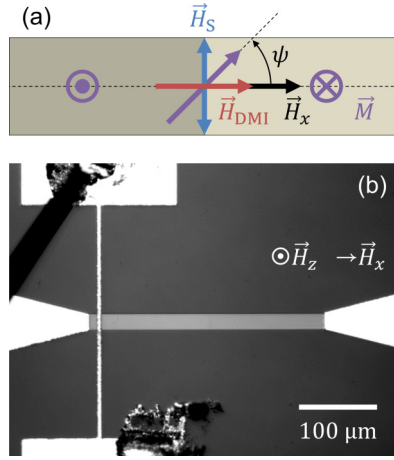


FIG. 5. (a) Schematic drawing of the experimental situation for the DW-based measurement. A domain is placed at center between two domains (areas with different colors) of opposite magnetization. The purple arrows represent the direction of magnetization inside the DW, with an angle  $\psi$  from the  $x$  axis. The red, blue, and black arrows show directions of  $H_{\text{DMI}}$ ,  $H_S$ , and  $H_x$ , respectively. (b) Optical image of the magnetic microwire for the  $\varepsilon_{\text{SOT}}$  scheme.

on SWs. For this measurement, two different schemes were employed, which are based on the spin-orbit torque (SOT) efficiency  $\varepsilon_{\text{SOT}}$  originally proposed by Haazen *et al.* [9] and based on the field-induced DW speed  $v_{\text{DW}}$  originally proposed by Je *et al.* [10]. We will denote these schemes as “ $\varepsilon_{\text{SOT}}$  scheme” and “ $v_{\text{DW}}$  scheme,” respectively, hereafter.

Both the schemes characterize the DW-chirality-dependent behaviors, where the DW chirality can be adjusted by applying external magnetic field. Figure 5(a) shows the angle  $\psi$  of the magnetization inside the DW, defined as the angle from the direction normal to the DW. The DW chirality can be then parametrized by  $\psi$ , where the Bloch-type DW chirality corresponds to  $\psi = \pm\pi/2$  and the Néel-type DW chirality corresponds to  $\psi = 0$  or  $\pi$ . The angle  $\psi$  is governed by the counterbalance between the DMI-induced effective field  $H_{\text{DMI}}$  (red arrow), DW anisotropy field  $H_S$  (blue arrow), and the external magnetic field  $H_x$  (black arrow). According to Refs. [6,7,10], the counterbalance at equilibrium provides the equation of  $\cos \psi$  as a function of  $H_x$  as given by

$$\cos \psi(H_x) = \begin{cases} \frac{H_x + H_{\text{DMI}}}{H_S} & \text{for } |H_x + H_{\text{DMI}}| < H_S \\ \pm 1 & \text{otherwise} \end{cases}, \quad (3)$$

with  $H_S (\equiv 4K_D/\pi M_S)$  that is required to achieve the Néel-type DW chirality, where  $K_D$  is the DW anisotropy energy density.

#### A. $\varepsilon_{\text{SOT}}$ scheme

The  $\varepsilon_{\text{SOT}}$  scheme can directly measure  $\cos \psi(H_x)$ . The spin-orbit torque induces an effective out-of-plane magnetic field  $H_z^{\text{SOT}}$  under injection of electric current. Since  $H_z^{\text{SOT}}$  is linearly proportional to the injected current density  $J$ , it is useful to define the spin-orbit torque efficiency  $\varepsilon_{\text{SOT}} (\equiv H_z^{\text{SOT}}/J)$  as the proportionality constant of the linear relation  $H_z^{\text{SOT}} = \varepsilon_{\text{SOT}} J$ . According to the spin-orbit torque theories [9,34],  $\varepsilon_{\text{SOT}}$  is proportional to the magnetization component longitudinal to the direction of  $J$ . In the present experimental situation that

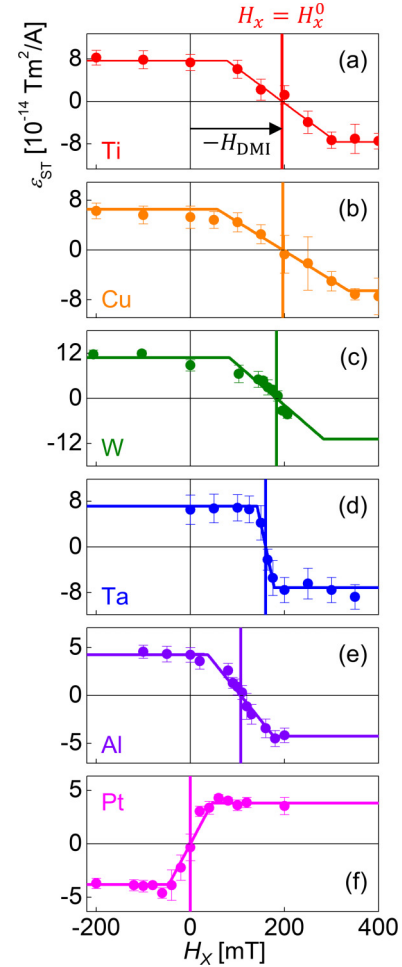


FIG. 6. Plots of  $\varepsilon_{\text{SOT}}$  as a function of  $H_x$  for the series of Pt/Co/ $X$  films with different  $X$  as denoted in each panel. The colored vertical lines designate the antisymmetry center.

$J$  is injected along the  $x$  axis as shown by Fig. 5(b),  $\varepsilon_{\text{SOT}}$  is proportional to the direction cosine of the magnetization along the  $x$  axis, leading to the equation

$$\varepsilon_{\text{SOT}}(\psi_0) = \varepsilon_{\text{SOT}}^0 \cos \psi, \quad (4)$$

with  $\varepsilon_{\text{SOT}}^0 \equiv \hbar\theta_{\text{SH}}/2eM_S t_{\text{Co}}$ , where  $\theta_{\text{SH}}$  is the net spin Hall angle of the system and  $t_{\text{Co}}$  is the thickness of the ferromagnetic Co layer. Then, by combining Eqs. (2) and (3),  $\varepsilon_{\text{SOT}}$  can be finally written as a function of  $H_x$  in the form of

$$\varepsilon_{\text{SOT}}(H_x) = \begin{cases} \varepsilon_{\text{SOT}}^0 \frac{H_x + H_{\text{DMI}}}{H_S} & \text{for } |H_x + H_{\text{DMI}}| < H_S \\ \pm \varepsilon_{\text{SOT}}^0 & \text{otherwise} \end{cases}. \quad (5)$$

Figure 6 shows the experimental confirmation of this prediction. Each panel plots  $\varepsilon_{\text{SOT}}$  with respect to  $H_x$  for the series of films with different  $X$  as denoted inside each panel. All the experimental results (symbols) agree well with the theoretical prediction (solid curves) of Eq. (5). The antisymmetry axis (colored vertical lines) indicates the magnetic-field strength  $H_x^0$ , which satisfies  $\varepsilon_{\text{SOT}}(H_x^0) = 0$ , i.e.,  $H_x^0 + H_{\text{DMI}} = 0$ . Therefore, one can quantify the magnitude of  $H_{\text{DMI}} (= -H_x^0)$  by measuring the antisymmetry center. The measured values of  $H_{\text{DMI}}$  are listed in Table I.

The DMI strengths  $D_{\text{DW}}$  are then estimated by the relation  $D_{\text{DW}} = (\lambda M_S) H_{\text{DMI}}$  with the DW width  $\lambda (= \sqrt{A/K_{\text{eff}}})$ , where  $A$  is the exchange stiffness constant and  $K_{\text{eff}}$  is the effective PMA constant. Here,  $D_{\text{DW}}$  refers to the DMI strengths on DWs, in distinction to the DMI strengths  $D_{\text{SW}}$  on SWs. In this calculation, the literature value of  $A (= 2.2 \times 10^{-11} \text{ J/m})$  for fcc Co [35,36] and the experimental values of  $K_{\text{eff}} (= \frac{1}{2} H_K M_S)$  are used, where  $H_K$  and  $M_S$  values were measured by a vibrating sample magnetometer [37]. The estimated values of  $D_{\text{DW}}$  are listed in Table I.

It is worthwhile to mention the possible artifacts in the  $\varepsilon_{\text{SOT}}$  scheme. The present scheme measures the effective magnetic field induced by current injection. Since the spin-transfer torque (STT) also induces the effective magnetic field under injection of current, the spin-transfer torque causes another efficiency  $\varepsilon_{\text{STT}}$ . Thus, the measured efficiency of the present scheme contains both contributions of  $\varepsilon_{\text{SOT}}$  and  $\varepsilon_{\text{STT}}$  (i.e.  $\varepsilon_{\text{ST}} = \varepsilon_{\text{SOT}} + \varepsilon_{\text{STT}}$  in Fig. 6). Though it has been known that  $\varepsilon_{\text{STT}}$  is negligibly small in comparison to  $\varepsilon_{\text{SOT}}$  in general, a sizable  $\varepsilon_{\text{STT}}$  begins to appear as the Co layer thickness decreases down to a few atomic monolayers [38]. Therefore, the appearance of  $\varepsilon_{\text{STT}}$  limits the lower bound of the thickness range valid for the  $\varepsilon_{\text{SOT}}$  scheme.

According to Ref. [38],  $\varepsilon_{\text{STT}}$  exhibits a symmetric variation for inversion with respect to  $H_x^0$ , which is far distinct from the antisymmetric variation of  $\varepsilon_{\text{SOT}}$ . Therefore, the degree

of artifacts due to a sizable  $\varepsilon_{\text{STT}}$  can be readily examined on the basis of the shape of measured efficiency variation, by checking whether the shape exhibits noticeable deviation from the typical antisymmetric variation. As seen from Fig. 6, the present series of films shows typical antisymmetric behaviors, confirming that  $\varepsilon_{\text{STT}}$  is negligible in this series of films and thus, the present scheme provides valid results in accordance with the measurement principles. For the case that a sizable  $\varepsilon_{\text{STT}}$  exists, an additional analysis is required to decompose the contributions of  $\varepsilon_{\text{STT}}$  and  $\varepsilon_{\text{SOT}}$  from several different measurements with opposite polarities as proposed by Ref. [38].

### B. $v_{\text{DW}}$ scheme

The  $v_{\text{DW}}$  scheme measures the DW-chirality-related phenomena in the DW speed  $v_{\text{DW}}$ . In the DW creep regime,  $v_{\text{DW}}$  follows the creep scaling criticality with respect to an out-of-plane magnetic field  $H_z$  as given by

$$v_{\text{DW}} = v_0 \exp[-\alpha H_z^{-1/4}], \quad (6)$$

where  $v_0$  is the characteristic speed and  $\alpha$  is the creep scaling constant. According to Ref. [10],  $\alpha$  depends on the DW energy density  $\sigma_{\text{DW}}$  with a power-law scaling in the form of  $\alpha \propto (\sigma_{\text{DW}})^{1/4}$ . Since  $\sigma_{\text{DW}}$  varies with the DW chirality, by applying the DW chirality in Eq. (3) to the  $\sigma_{\text{DW}}$  equation, one obtains  $\sigma_{\text{DW}}$  as a function of  $H_x$  as given by

$$\sigma_{\text{DW}}(H_x) = \begin{cases} \sigma_0 - 2\lambda K_D \left( \frac{H_x + H_{\text{DMI}}}{H_S} \right)^2 & \text{for } |H_x + H_{\text{DMI}}| < H_S \\ \sigma_0 + 2\lambda K_D - \pi \lambda M_S |H_x + H_{\text{DMI}}| & \text{otherwise} \end{cases}, \quad (7)$$

where  $\sigma_0$  is the Bloch-type DW energy density. In contrast to the antisymmetric variation of  $\varepsilon_{\text{SOT}}(H_x)$  in Eq. (5),  $v_{\text{DW}}(H_x)$  exhibits symmetric variation for inversion with respect to the symmetry center  $H_x^0 (= -H_{\text{DMI}})$ .

Figure 7 shows the experimental confirmation of this prediction. Each panel plots  $v_{\text{DW}}$  in a logarithmic scale with respect to  $H_x$  for another series of Pt/Co/Pt films with different Co layer thickness as denoted inside each panel. The first two panels for the films with thinner Co layers (0.3 and 0.4 nm) exhibit that the experimental results (symbols) agree well with the theoretical prediction of the symmetric  $v_{\text{DW}}$  variation. The symmetry center (red vertical lines) indicates the magnetic-field strength  $H_x^0$  and therefore, one can quantify the magnitude of  $H_{\text{DMI}} (= -H_x^0)$  by measuring the symmetry center.

It is also worthwhile to discuss the possible artifacts in the  $v_{\text{DW}}$  scheme. Recent studies have shown that there exists additional asymmetry in the  $v_{\text{DW}}$  variation [39]. Such additional asymmetry messes up the symmetric  $v_{\text{DW}}$  variation by shifting the apparent minimum from the symmetry center, resulting in severe inaccuracy in determination of  $H_{\text{DMI}}$ . Though the exact origins of the additional asymmetry remain under debate [39–46], it has been experimentally observed that a larger additional asymmetry appears in thicker magnetic layers as shown by the lower panels of Fig. 7. In consequence, the additional asymmetry limits the upper bound of the thickness range valid for the  $v_{\text{DW}}$  scheme.

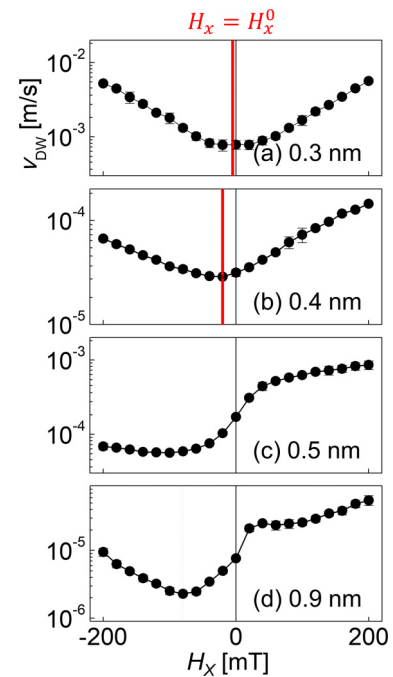


FIG. 7. Plot of  $v_{\text{DW}}$  as a function of  $H_x$  for the series of Pt/Co/Pt films with different Co layer thickness as denoted in each panel. The red vertical lines designate the symmetry center.

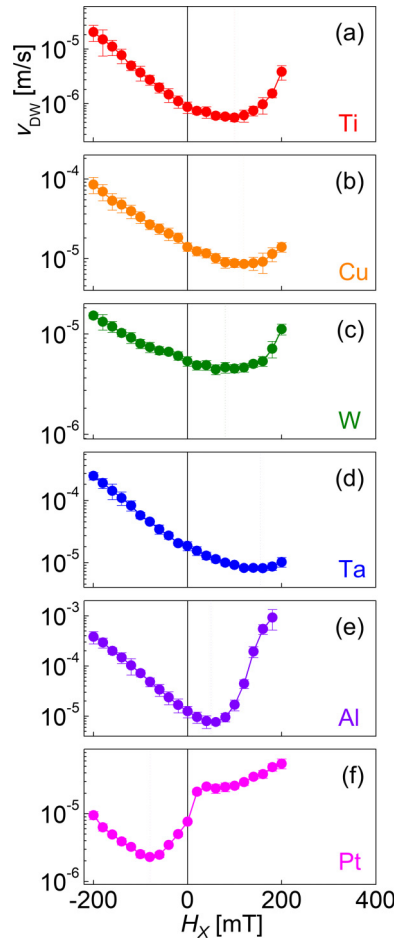


FIG. 8. Plot of  $v_{DW}$  as a function of  $H_x$  for the series of Pt/Co/ $X$  films with different  $X$  as denoted in each panel.

In the  $v_{DW}$  scheme, it is therefore strongly recommended to check priorly whether the measured  $v_{DW}$  variation presents a clear shape of symmetry, before quantifying the magnitude of  $H_{DMI}$ . Without clear symmetry, the magnetic field for the apparent  $v_{DW}$  minimum does not guarantee valid results. Figure 8 plots  $v_{DW}$  in a logarithmic scale with respect to  $H_x$  for the series of Pt/Co/ $X$  films with different  $X$  as denoted inside each panel. As seen from the plots, most curves do not show clear symmetry in the  $v_{DW}$  variation, indicating the existence of sizable additional asymmetries. Since there is no symmetry center, it is not possible to determine  $H_{DMI}$  for this series of films. Therefore, the  $v_{DW}$  scheme is not suitable for this series of films, of which the ferromagnetic layer thickness might be thicker than the upper bound of the thickness range valid for this scheme.

## V. COMPARISON BETWEEN DMI STRENGTHS ON SWs AND DWs

Finally, a quantitative comparison of the DMI between the DW dynamics and the SW dynamics was investigated. Figure 9 plots the measured values of  $D_{SW}$  with respect to  $D_{DW}$  for the series of films with various  $X$  [47]. The plot clearly shows a great quantitative agreement between the magnitudes of  $D_{DW}$  and  $D_{SW}$  [48]. This observation manifests

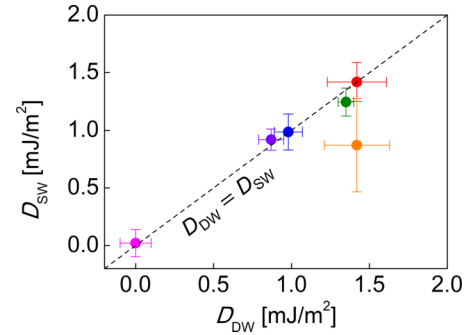


FIG. 9. Plot of  $D_{SW}$  with respect to  $D_{DW}$ . The dashed line guides the eyes for the relation  $D_{DW} = D_{SW}$ .

that the DMI strength is the same for both cases of SWs and DWs, regardless of their distinct situations: The former corresponds to small deviation from uniform magnetization and the latter has largely varying nonuniform magnetization. In addition, the same DMI strength from two different schemes confirms the reliability of the present measurement schemes and thus, provides a way towards establishing measurement standards.

## VI. SUMMARY

We conclude with a discussion of the experimental conditions applicable for each measurement scheme and the cardinal rules for selecting the most appropriate scheme.

### A. Suitable range of ferromagnetic layer thickness for each measurement scheme

Both the  $\varepsilon_{SOT}$  and  $v_{DW}$  schemes have a prerequisite of clean DWs with low roughness and clear DW motion in magnetization process. Otherwise, the position of DWs cannot be unambiguously detected as well, as local deviation of the DW chirality in rough DWs leads to significant inaccuracies in the DMI determination. This prerequisite imposes an upper limit on the thickness of ferromagnetic layers, since the magnetization process changes from the DW-motion phase to the dendrite phase as the thickness increases.

For the  $v_{DW}$  schemes, the applicable thickness range is further limited due to the appearance of the additional  $v_{DW}$  asymmetry [39] as discussed in Sec. IV B. In practice, therefore, the suitable thickness range of the  $v_{DW}$  scheme is limited safely within a few atomic monolayers. Contrarily, the  $\varepsilon_{SOT}$  scheme is not applicable for this thickness range, since a sizable STT [38] has been observed in this thickness range as discussed in Sec. IV A. Therefore, the suitable thickness ranges of these schemes are separate with a little overlap, as illustrated by Fig. 10 with a schematic drawing. In Fig. 10, the  $v_{DW}$  scheme (purple area) covers the thickness range smaller than the thickness for the appearance of the additional  $v_{DW}$  asymmetry (purple vertical line), whereas the  $\varepsilon_{SOT}$  scheme (blue area) covers the thickness range between the thicknesses for appearance of the sizable STT (blue vertical line) and the dendrite phase (black vertical line).

On the other hand, the BLS scheme has a prerequisite of strong in-plane magnetic field, which has to be sufficiently

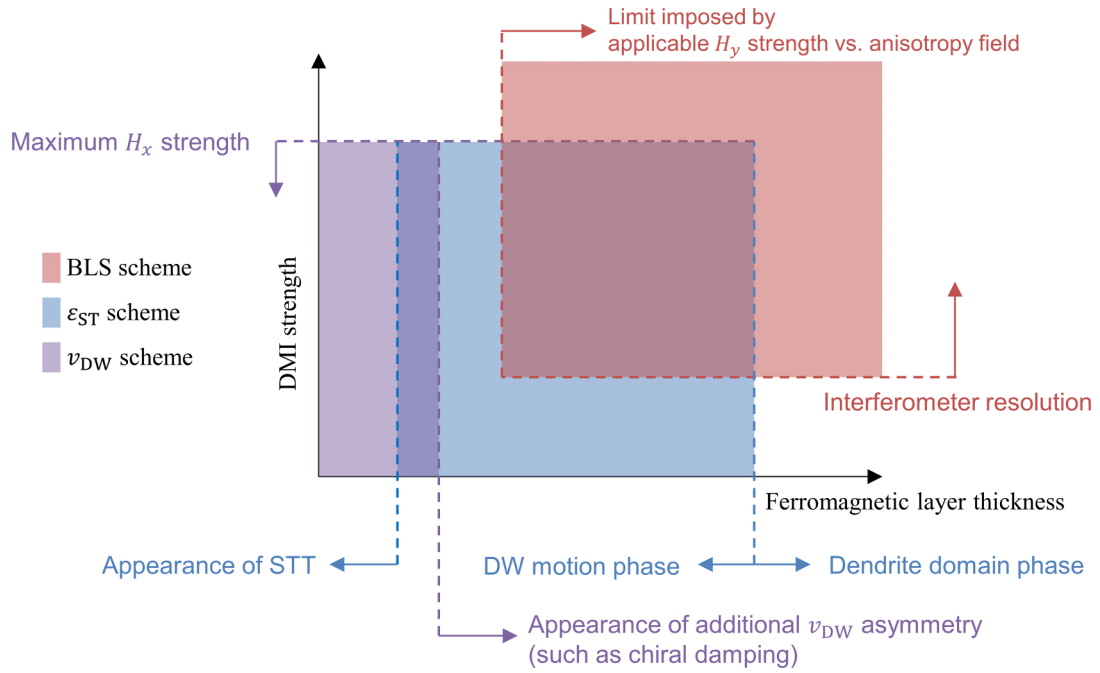


FIG. 10. Schematic drawing on conceptual hierarchy of the measurement schemes. Each colored area shows the appropriate range for each scheme, in terms of the ferromagnetic layer thickness and the DMI strength. The BLS scheme (red area) covers the thickness range thicker than the lower limit imposed by the applicable maximum magnetic field strength (red vertical line) and the DMI strength range larger than the interferometer resolution (red horizontal line). The  $\epsilon_{ST}$  scheme covers the thickness range between the thicknesses of appearance of the sizable STT (blue vertical line) and the dendrite phase (black vertical line) as well as the  $H_{DMI}$  range smaller than the applicable magnetic-field strength (blue horizontal line). The  $\nu_{DW}$  scheme covers the thickness range smaller than the thickness for the appearance of the additional  $\nu_{DW}$  asymmetry (purple vertical line) and the  $H_{DMI}$  range smaller than the applicable magnetic-field strength (blue horizontal line). The dashed box shows the area overlapping between the  $\epsilon_{ST}$  and BLS schemes, which the present series of Pt/Co/X films belongs to.

stronger than the anisotropy field [15–18]. This prerequisite imposes the lower limit on the thickness range of the ferromagnetic layer, since thinner layers have stronger anisotropy with inverse proportionality due to the interfacial nature. Therefore, in Fig. 10, the BLS scheme (red area) covers the thickness range thicker than the lower limit imposed by the applicable maximum magnetic-field strength (red vertical line).

### B. Suitable range of DMI strength for each measurement scheme

The  $\epsilon_{ST}$  and  $\nu_{DW}$  schemes measure the magnetic field at the antisymmetry [9,34] and symmetry [10,39] centers. Since such measurement is done within the range of the applied magnetic field, the maximum measurable strength of  $H_{DMI}$  is limited by the maximum strength of the applied magnetic field. There is no definite limit on the minimum measurable strength except the statistical accuracy, since the antisymmetry and symmetry centers can be placed at any place in the measurement range. Therefore, in Fig. 10, both the schemes cover the  $H_{DMI}$  range smaller than the applicable magnetic-field strength (blue horizontal line) [49].

On the other hand, for the BLS scheme, the DMI is quantified from the frequency shift and thus, the frequency resolution of the tandem Fabry-Perot interferometer practically imposes the lower limit on the measurable DMI strength. Therefore, in Fig. 10, the BLS scheme covers the DMI

strength range larger than the interferometer resolution (red horizontal line).

### C. Measured quantities and experimental prerequisites

The  $\epsilon_{ST}$  and  $\nu_{DW}$  schemes quantify the values of  $H_{DMI}$  directly from the magnetic field at the antisymmetry and symmetry centers. Therefore, these schemes are useful for the cases that  $H_{DMI}$  directly appears in the governing equation. However, the DMI strength has to be estimated with additional information of the DW width and the saturation magnetization. Since it is not easy to determine the DW width experimentally, it is common to estimate the DW width based on the ansatz of the Bloch-type DW width as discussed in Sec. IV A, which might be accompanied by additional experimental inaccuracies in the DMI strength.

On the other hand, the BLS scheme measures the frequency shift and then estimates the DMI strength by using the values of the wave vector and saturation magnetization. Since these values can be easily determined experimentally, this scheme provides a better accuracy in determination of the DMI strength. However, contrarily, the estimation of  $H_{DMI}$  requires additional information as mentioned above.

The BLS and  $\nu_{DW}$  schemes can be applied to films without any patterning process, whereas the  $\epsilon_{ST}$  scheme requires additional preparation process of wire patterns to inject electric current into the structure. Therefore, for the  $\epsilon_{ST}$  scheme, care should be taken in the patterning process to avoid undesirable changes in the properties of films. It

is also worthwhile to compare the measurement times of each measurement scheme. The BLS-scheme experiments are performed by a single procedure of measuring the reflected light intensity with sweeping the SW frequency. Similarly, the  $v_{DW}$ -scheme experiments are performed by a single procedure of measuring  $v_{DW}$  with sweeping the in-plane magnetic field. In contrast to these schemes, the  $\varepsilon_{SOT}$ -scheme experiments require two-step procedures by sweeping both the injected current density and in-plane magnetic field. Therefore, the  $\varepsilon_{SOT}$ -scheme experiments generally take longer than the others.

#### D. Overview

Figure 10 finally summarizes the schematic overview on conceptual hierarchy of the measurement schemes. Each scheme has its own appropriate measurable range in terms of the ferromagnetic layer thickness and the DMI strength. In general, the DW-based schemes are better for thinner ferromagnetic layers and weaker DMI strength, whereas the SW-based scheme is better for thicker ferromagnetic layers and stronger DMI strength. Outside the appropriate measurable range, each scheme might provide misleading results. To avoid such misleading results, it is therefore essential to primarily check whether the measurement data follow the typical symmetric and antisymmetric behaviors proposed by the measurement principles.

The present series of Pt/Co/X films belongs to the area overlapping between the areas valid for the BLS and  $\varepsilon_{SOT}$  schemes and thus, it was possible to directly compare their results. The quantitative accordance between the DW- and SW-based mechanisms indicates that the same DMI mechanism appears in both the situations of largely varying nonuniform magnetization and small deviation in uniform magnetization.

In addition, the present observation confirms the reliabilities of the recently developed various measurement schemes and thus, provide a way towards establishing measurement standards.

#### ACKNOWLEDGMENTS

This work was supported by the Samsung Science & Technology Foundation (Grant No. SSTF-BA1802-07) and the National Research Foundations of Korea (NRF) grant that was funded by the Ministry of Science, ICT and Future Planning of Korea (MSIP) (Grants No. 2015M3D1A1070465, and No. 2017R1A2B3002621). D.-Y.K., Y.-K.P., D.-H.K., and B.-C.M. were supported by the KIST institutional program (Grant No. 2E29410) and National Research Council of Science & Technology (Grant No. CAP-16-01-KIST). J.-S.K. was supported by the DGIST R&D Programs of the Ministry of Science and ICT (Grant No. 18-NT-01). D.-H.K. and J.C. were supported by Overseas Researcher under the Postdoctoral Fellowship of JSPS (Grants No. P16314 and No. P16362). D.-H.K. was supported by NST Research Fellowship for Young Scientist of the National Research Council of Science & Technology (NST) and by the POSCO Science Fellowship of POSCO TJ Park Foundation.

D.-Y.K. planned and designed the experiment; S.-B.C. and C.-Y.Y. supervised the study. D.-Y.K., N.-H.K., Y.-S.N., J.-S.K., and J.J. carried out the measurements. M.-H.P., Y.-K.P., and B.-C.M. prepared the samples. D.-Y.K., N.-H.K., J.C., D.-H.K., J.-S.K., S.-B.C., and C.-Y.Y. performed the analysis. D.-Y.K., S.-B.C., and C.-Y.Y. wrote the manuscript. All authors discussed the results and commented on the manuscript.

D.-Y.K. and N.-H.K. contributed equally to this work.

- 
- [1] I. Dzyaloshinsky, *J. Phys. Chem. Solids* **4**, 241 (1958).  
 [2] T. Moriya, *Phys. Rev.* **120**, 91 (1960).  
 [3] A. Fert, V. Cros, and J. Sampaio, *Nat. Nanotechnol.* **8**, 152 (2013).  
 [4] T. Schulz, R. Ritz, A. Bauer, M. Halder, M. Wagner, C. Franz, C. Pfleiderer, K. Everschor, M. Garst, and A. Rosch, *Nat. Phys.* **8**, 301 (2012).  
 [5] S. Mühlbauer, B. Binz, F. Jonietz, C. Pfleiderer, A. Rosch, A. Neubauer, R. Georgii, and P. Böni, *Science* **323**, 915 (2009).  
 [6] A. Thiaville, S. Rohart, E. Jué, V. Cros, and A. Fert, *Europhys. Lett.* **100**, 57002 (2012).  
 [7] M. Heide, G. Bihlmayer, and S. Blügel, *Phys. Rev. B* **78**, 140403(R) (2008).  
 [8] H. Yang, A. Thiaville, S. Rohart, A. Fert, and M. Chshiev, *Phys. Rev. Lett.* **115**, 267210 (2015).  
 [9] P. P. J. Haazen, E. Murè, J. H. Franken, R. Lavrijsen, H. J. M. Swagten, and B. Koopmans, *Nat. Mater.* **12**, 299 (2013).  
 [10] S.-G. Je, D.-H. Kim, S.-C. Yoo, B.-C. Min, K.-J. Lee, and S.-B. Choe, *Phys. Rev. B* **88**, 214401 (2013).  
 [11] A. Hrabec, N. A. Porter, A. Wells, M. J. Benitez, G. Burnell, S. McVitie, D. McGrouther, T. A. Moore, and C. H. Marrows, *Phys. Rev. B* **90**, 020402(R) (2014).  
 [12] D.-Y. Kim, D.-H. Kim, J. Moon, and S.-B. Choe, *Appl. Phys. Lett.* **106**, 262403 (2015).  
 [13] D.-S. Han, N.-H. Kim, J.-S. Kim, Y. Yin, J.-W. Koo, J. Cho, S. Lee, M. Klaui, H. J. M. Swagten, B. Koopmans, and C.-Y. You, *Nano Lett.* **16**, 4438 (2016).  
 [14] S. Kim, P.-H. Jang, D.-H. Kim, M. Ishibashi, T. Taniguchi, T. Moriyama, K.-J. Kim, K.-J. Lee, and T. Ono, *Phys. Rev. B* **95**, 220402(R) (2017).  
 [15] J. Cho, N.-H. Kim, S. Lee, J.-S. Kim, R. Lavrijsen, A. Solignac, Y. Yin, D.-S. Han, N. J. J. van Hoof, H. J. M. Swagten, B. Koopmans, and C.-Y. You, *Nat. Commun.* **6**, 7635 (2015).  
 [16] K. Di, V. L. Zhang, H. S. Lim, S. C. Ng, M. H. Kouk, J. Yu, J. Yoon, X. Qiu, and H. Yang, *Phys. Rev. Lett.* **114**, 047201 (2015).  
 [17] H. T. Nembach, J. M. Shaw, M. Weiler, E. Jué, and T. J. Silva, *Nat. Phys.* **11**, 825 (2015).  
 [18] J.-M. Lee, C. Jang, B.-C. Min, S.-W. Lee, K.-J. Lee, and J. Chang, *Nano Lett.* **16**, 62 (2015).  
 [19] M. Belmeguenai, J.-P. Adam, Y. Roussigné, S. Eimer, T. Devolder, J.-V. Kim, S. M. Cherif, A. Stashkevich, and A. Thiaville, *Phys. Rev. B* **91**, 180405(R) (2015).



- [20] M. Belmeguenai, M. S. Gabor, Y. Roussigné, A. Stashkevich, S. M. Chérif, F. Zighem, and C. Tiusan, *Phys. Rev. B* **93**, 174407 (2016).
- [21] S. Tacchi, R.E. Troncoso, M. Ahlberg, G. Gubbiotti, M. Madami, J. Åkerman, and P. Landeros, *Phys. Rev. Lett.* **118**, 147201 (2017).
- [22] X. Ma, G. Yu, X. Li, T. Wang, D. Wu, K. S. Olsson, Z. Chu, K. An, J. Q. Xiao, K. L. Wang, and X. Li, *Phys. Rev. B* **94**, 180408(R) (2016).
- [23] R. Soucaille, M. Belmeguenai, J. Torrejon, J.-V. Kim, T. Devolder, Y. Roussigné, S.-M. Chérif, A. A. Stashkevich, M. Hayashi, and J.-P. Adam, *Phys. Rev. B* **94**, 104431 (2016).
- [24] K. Di, V. L. Zhang, H. S. Lim, S. C. Ng, M. H. Kuok, X. Qiu, and H. Yang, *Appl. Phys. Lett.* **106**, 052403 (2015).
- [25] X. Ma, G. Yu, S. A. Razavi, S. S. Sasaki, X. Li, K. Hao, S. H. Tolbert, K. L. Wang, and X. Li, *Phys. Rev. Lett.* **119**, 027202 (2017).
- [26] A. K. Chaurasiya, C. Banerjee, S. Pan, S. Sahoo, S. Choudhury, J. Sinha, and A. Barman, *Sci. Rep.* **6**, 32592 (2016).
- [27] R. M. Rowan-Robinson, A. A. Stashkevich, Y. Roussigné, M. Belmeguenai, S.-M. Chérif, A. Thiaville, T. P. A. Hase, A. T. Hindmarch, and D. Atkinson, *Sci. Rep.* **7**, 16835 (2017).
- [28] A. K. Chaurasiya, S. Choudhury, J. Sinha, and A. Barman, *Phys. Rev. Appl.* **9**, 014008 (2018).
- [29] M. Belmeguenai, H. Bouloussa, Y. Roussigné, M. S. Gabor, T. Petrisor, Jr., C. Tiusan, H. Yang, A. Stashkevich, and S. M. Chérif, *Phys. Rev. B* **96**, 144402 (2017).
- [30] H. Bouloussa, J. Yu, Y. Roussigné, M. Belmeguenai, A. Stashkevitch, H. Yang, and S. M. Chérif, *J. Phys. D: Appl. Phys.* **51**, 225005 (2018).
- [31] L. Camosi, S. Rohart, O. Fruchart, S. Pizzini, M. Belmeguenai, Y. Roussigné, A. Stashkevich, S. M. Cherif, L. Ranno, M. de Santis, and J. Vogel, *Phys. Rev. B* **95**, 214422 (2017).
- [32] R. W. Damon and J. R. Eshbach, *Phys. Chem. Solids* **19**, 308 (1961).
- [33] B. Heinrich, J. F. Cochran, M. Kowalewski, J. Kirschner, Z. Celinski, A. S. Arrott, and K. Myrtle, *Phys. Rev. B* **44**, 9348 (1991).
- [34] J. H. Franken, M. Herps, H. J. M. Swagten, and B. Koopmans, *Sci. Rep.* **4**, 5248 (2014).
- [35] P. J. Metaxas, J. P. Jamet, A. Mougin, M. Cormier, J. Ferre, V. Baltz, B. Rodmacq, B. Dieny, and R. L. Stamps, *Phys. Rev. Lett.* **99**, 217208 (2007).
- [36] See Supplemental Material at <http://link.aps.org/supplemental/10.1103/PhysRevB.100.224419>, Sec. I for experimental measurement of exchange stiffness.
- [37] See Supplemental Material at <http://link.aps.org/supplemental/10.1103/PhysRevB.100.224419>, Sec. II for measurement of  $K_{\text{eff}}$  by means of the BLS.
- [38] S.-G. Je, S.-C. Yoo, J.-S. Kim, Y.-K. Park, M.-H. Park, J. Moon, B.-C. Min, and S.-B. Choe, *Phys. Rev. Lett.* **118**, 167205 (2017).
- [39] D.-Y. Kim, M.-H. Park, Y.-K. Park, J.-S. Kim, Y.-S. Nam, H.-C. Choi, D.-H. Kim, S.-G. Je, B.-C. Min, and S.-B. Choe, *NPG Asia Mater.* **10**, e464 (2018).
- [40] R. Lavrijsen, D. M. F. Hartmann, A. van den Brink, Y. Yin, B. Barcones, R. A. Duine, M. A. Verheijen, H. J. M. Swagten, and B. Koopmans, *Phys. Rev. B* **91**, 104414 (2015).
- [41] E. Jué, C. K. Safeer, M. Drouard, A. Lopez, P. Balint, L. Buda-Prejbeanu, O. Boule, S. Auffret, A. Schuhl, A. Manchon, I. M. Miron, and G. Gaudin, *Nat. Mater.* **15**, 272 (2016).
- [42] C. A. Akosa, I. M. Miron, G. Gaudin, and A. Manchon, *Phys. Rev. B* **93**, 214429 (2016).
- [43] D.-Y. Kim, D.-H. Kim, and S.-B. Choe, *Appl. Phys. Express* **9**, 053001 (2016).
- [44] D. Lau, V. Sundar, J.-G. Zhu, and V. Sokalski, *Phys. Rev. B* **94**, 060401(R) (2016).
- [45] D.-H. Kim, D.-Y. Kim, S.-C. Yoo, B.-C. Min, and S.-B. Choe, *Phys. Rev. B* **99**, 134401 (2019).
- [46] J. P. Pellegren, D. Lau, and V. Sokalski, *Phys. Rev. Lett.* **119**, 027203 (2017).
- [47] Y.-K. Park, D.-Y. Kim, J.-S. Kim, Y.-S. Nam, M.-H. Park, B.-C. Min, and S.-B. Choe, *NPG Asia Mater.* **10**, 995 (2018).
- [48] See Supplemental Material at <http://link.aps.org/supplemental/10.1103/PhysRevB.100.224419>, Sec. III for discussion on the large uncertainty of  $D_{\text{sw}}$  for  $X = \text{Cu}$  film.
- [49] D.-H. Kim, S.-C. Yoo, D.-Y. Kim, B.-C. Min, and S.-B. Choe, *Sci. Rep.* **7**, 45498 (2017).